The Astrophysical Journal Letters, 996:L17 (10pp), 2026 January 1 https://doi.org/10.3847/2041-8213/ae2868

Water Vapor Emission at the Warm Cavity Wall of the HD 100546 Disk as Revealed by ALMA

Rampinelli Luna[1], Facchini Stefano[1], Leemker Margot[1], Isella Andrea[2,3], Curone Pietro[4], Benisty Myriam[5], Humphreys Elizabeth[6,7], and Testi Leonardo[8]

[1] Dipartimento di Fisica, Università degli Studi di Milano, Via Celoria 16, 20133 Milano, Italy; luna.rampinelli@unimi.it
[2] Department of Physics and Astronomy, Rice University, 6100 Main Street, MS-108, Houston, TX 77005, USA
[3] Rice Space Institute, Rice University, 6100 Main Street, MS-108, Houston, TX 77005, USA
[4] Departamento de Astronomía, Universidad de Chile, Camino El Observatorio 1515, Las Condes, Santiago, Chile
[5] Max-Planck Institute for Astronomy (MPIA), Königstuhl 17, 69117 Heidelberg, Germany
[6] Joint ALMA Observatory (JAO), Alonso de Córdova 3107, Vitacura 763-0355, Casilla 19001, Santiago, Chile
[7] European Southern Observatory (ESO), Alonso de Córdova 3107, Vitacura 763-0355, Santiago, Chile
[8] Alma Mater Studiorum Universitá di Bologna, Dipartimento di Fisica e Astronomia (DIFA), Via Gobetti 93/2, 40129 Bologna, Italy

Received 2025 September 17; revised 2025 November 19; accepted 2025 December 4; published 2025 December 30

Abstract

We present spatially resolved Atacama Large Millimeter/submillimeter Array (ALMA) observations of the water line at 183 GHz in the disk around the Herbig star HD 100546. The water vapor emission peaks at the inner edge of the warm dust cavity, located ∼15 au from the central star. We attribute this to thermal desorption at the water snow line, shifted outward at the dust cavity wall directly heated by the intense radiation. This represents the first spatially resolved image of the water snow line using ALMA observations of the main water isotopologue in a protoplanetary disk. The water emission morphology peaking inside the first dust ring is consistent with previous ALMA detections of oxygen-bearing complex organic molecules in the disk, including thermally desorbed methanol. These findings signal that warm cavities of transition disks provide ideal targets to directly reconstruct the spatial distribution of water vapor and the snow line location with ALMA and directly connect water vapor emission to ice desorption of complex organic species.

Unified Astronomy Thesaurus concepts: Protoplanetary disks (1300); Planet formation (1241); Water vapor (1791); Radio interferometry (1346)

1. Introduction

Water is of primary interest in astronomy, as it plays a fundamental role in the emergence of life on Earth, liquid water being an efficient solvent that facilitates the development of chemical complexity. Understanding how water was delivered to Earth is a central question in astronomy (A. Morbidelli et al. 2012). However, answering this question is challenging, as it is closely intertwined with the complex chemical and physical history of the building blocks of planets and their interplay with water in their natal environments, the protoplanetary disks (E. F. van Dishoeck et al. 2021).

Water observations in the protoplanetary disk stage are extremely valuable, as they offer a unique opportunity to observationally characterize the link between the atmospheric composition of the evolved exoplanetary population and their birthplace (A. J. Cridland et al. 2016). In addition, the water in these sources is likely formed before the central star, thus injecting all systems with a similar water abundance at the time of their formation (A. Andreu et al. 2023; J. J. Tobin et al. 2023; M. Leemker et al. 2025). Being a primary oxygen carrier, water plays a crucial role in determining the chemical makeup of the planet-forming material by often dominating the C/O ratio in the gas and ice phases (K. I. Öberg et al. 2011; K. I. Öberg et al. 2023; C. Eistrup et al. 2018). Beyond the water snow line, at a midplane temperature below ∼150 K, the water freezes on dust grains, enriching the ice with oxygen sequestered from the gas phase. The location of the snow line not only regulates the chemical composition of the disk reservoir but also promotes planet formation by facilitating grain growth and coagulation (D. Schoonenberg & C. W. Ormel 2017; J. Drążkowska et al. 2023).

Water observations in disks have been performed mainly with infrared campaigns and have confirmed the main water reservoirs predicted by disk thermochemical models (see, e.g., K. M. Pontoppidan et al. 2010; A. Banzatti et al. 2017; E. F. van Dishoeck et al. 2021, and references therein). Water gas is expected in three main regions in protoplanetary disks: (1) *Inside the water snow line, typically within a few astronomical units from the central star.* This is a warm reservoir of thermally desorbed water at temperatures above ∼150 K, with high abundances typically $\gtrsim 10^{-4}$ (P. Woitke et al. 2009; E. F. van Dishoeck et al. 2014). (2) *In the outer disk.* This is the cold component ($T \lesssim 100$ K) photodesorbed from icy grains, at intermediate layers where UV photons can penetrate. The abundance can reach up to 10^{-6}, and it is regulated by photodissociation and water self-shielding (E. A. Bergin et al. 2010; M. R. Hogerheijde et al. 2011). (3) *In the disk surface layer.* This is the hot component reformed in the gas phase at $T \gtrsim 300$ K. The high temperature required to unlock the gas-phase reaction pushes this region to higher layers, where the abundance can reach up to 10^{-4} as a result of the balance between photodissociation and self-shielding (T. Bethell & E. Bergin 2009). We refer the reader to E. F. van Dishoeck et al. (2021) and L. M. Pirovano et al. (2022) for a detailed description.

The first characterization of the water emission in protoplanetary disks was provided by IR campaigns with Spitzer, revealing correlations with stellar and disk properties, such as the stellar temperature and luminosity, accretion luminosity, disk dust mass, and size, but also dynamical processes such as the inward drift of icy pebbles (see, e.g., K. M. Pontoppidan et al. 2010; C. Salyk et al. 2011; J. R. Najita et al. 2013; A. Banzatti et al. 2020). Higher-resolution water spectra of the inner disk of protoplanetary disks obtained with the JWST revealed multiple temperature contributions associated with different water reservoirs (A. Banzatti et al. 2023b; I. Kamp et al. 2023), with the component consistent with the water sublimation temperature becoming more prominent at longer wavelengths ($\sim$23 μm, A. Banzatti et al. 2023a; M. Temmink et al. 2024). The cold water reservoir photodesorbed in the outer disk was detected by Herschel in the disks of TW Hya and HD 100546, revealing a weaker emission than previously predicted by models, as a result of the settling of icy grains over time (E. A. Bergin et al. 2010).

However, IR observations with current facilities lack the spatial resolution to resolve the water emission and directly constrain the snow line location, which is typically within only a few astronomical units for T Tauri stars and within $\sim$10 au for Herbig stars (P. Woitke et al. 2009; S. Notsu et al. 2017). J. J. Tobin et al. (2023) showed the first direct constraint of the water snow line location (at $\sim$80 au) from Atacama Large Millimeter/submillimeter Array (ALMA) observations of heavier water isotopologues in the disk around the outbursting V883 Ori star. S. Facchini et al. (2024) showed the first spatially and spectrally resolved ALMA observations of the main water vapor isotopologue in the protoplanetary disk of HL Tau. These results demonstrate the potential of ALMA in revealing the content, distribution, and location of the snow line of water vapor in disks. However, even though less important than in the IR, dust absorption can occult millimeter-wave water line emission arising from the disk midplane. Further imaging of water transitions at millimeter wavelengths in protoplanetary disks with optically thin inner regions can circumvent this problem (M. Leemker et al. 2025a).

In this work, we present the first spatially resolved ALMA observations of water vapor in a disk hosting a wide dust cavity. The source is described in Section 2, while observations used to perform the analysis, self-calibration, and image reconstruction are outlined in Section 3. We discuss the main results in Section 4 and summarize the main conclusions in Section 5.

2. The Source

HD 100546 is a Herbig star ($M_\star = 2.4\ M_\odot$, C. Walsh et al. 2017; $L_\star = 23.5\ L_\odot$, M. Vioque et al. 2018), at a distance of 110 pc (Gaia Collaboration et al. 2016, 2023). Two dust rings at $\sim$25 and $\sim$200 au have been detected in ALMA continuum observations (C. Walsh et al. 2014; J. E. Pineda et al. 2019; D. Fedele et al. 2021), while scattered light observations revealed small- and large-scale spiral arm structures (A. Garufi et al. 2016; K. B. Follette et al. 2017; E. Sissa et al. 2018). Both wide-orbit and close-in forming planet candidates have been suggested from submillimeter and infrared observations, asymmetric SO emission, and CO kinematic signatures (T. Currie et al. 2015; E. Sissa et al. 2018; S. D. Brittain et al. 2019; S. Casassus & S. Pérez 2019; J. E. Pineda et al. 2019; S. Pérez et al. 2020; A. S. Booth et al. 2023).

HD 100546 shows a line-rich spectrum with a variety of molecules detected with ALMA, among which complex organic molecules (COMs), such as methanol and methyl formate, show ring shape emission and/or azimuthal variations (A. S. Booth et al. 2023; L. Keyte et al. 2023; A. S. Booth et al. 2024; M. Leemker et al. 2024; L. Evans et al. 2025). In particular, methanol has an excitation temperature of $\sim$152 K inside 110 au, which is consistent with thermal desorption origin (L. Evans et al. 2025). Thermally desorbed water is therefore expected to be detected in the same region as methanol, as they have similar sublimation temperatures (V. Wakelam et al. 2017; M. Minissale et al. 2022). M. Leemker et al. (2024) modeled the HD 100546 disk with DALI (S. Bruderer et al. 2012, 2013) to reproduce ALMA line emission observations, and predicted the location of the snow line to be at $\sim$15 au, at the inner edge of the first dust ring.

Gas-phase water was previously detected in the disk around HD 100546 with Herschel (E. F. van Dishoeck et al. 2021; L. M. Pirovano et al. 2022). Both cold and warm lines with upper state energies ranging from $\sim$50 to $\sim$1000 K were targeted, but only the two cold lines at 557 GHz ($E_\mathrm{u} = 61$ K) and 1113 GHz ($E_\mathrm{u} = 53$ K) were detected and attributed to the cold photodesorbed water reservoir. The emitting region was inferred to be outside 40 au from the spectrally resolved line profiles (E. F. van Dishoeck et al. 2021).

L. M. Pirovano et al. (2022) modeled the Herschel observations of HD 100546 using DALI (S. Bruderer et al. 2012; S. Bruderer 2013) and constrained the water abundance in the three reservoirs discussed in Section 1. Their fiducial model predicts low water abundances in the thermally desorbed component ($<10^{-9}$) and in the hot reservoir formed in the gas phase ($<10^{-10}$), while the photodesorbed component at intermediate layers outside the dust ring at $\sim$40 au needs to be relatively abundant ($\sim 3 \times 10^{-9}$) to reproduce the observations.

Finally, M. Honda et al. (2016) detected an absorption feature at 3 μm with Gemini in the HD 100546 disk, associated with water ice in the surface layer in the outer gap between 40 and 120 au, which is in line with the results presented by L. M. Pirovano et al. (2022).

3. Observations

In this Letter, we analyzed ALMA band 5 observations of HD 100546 from project 2023.1.01431.S (PI: S. Facchini), which covers the $H_2O3_{1,3}$–$2_{2,0}$ line at $\nu = 183.310$ GHz. The observations consist of three execution blocks (EBs), obtained in C-5 configuration on 2024 June 30 (EB0 and EB1) and 2024 July 2 (EB2), with a maximum baseline of 2.5 km. The time on source for each EB was 47 minutes, for a total of 2.35 hr in exquisite weather conditions corresponding to precipitable water vapor (PWV) ranging from 0.21 to 0.45 mm across the EBs. The spectral setup is made of two spectral windows (spws) centered on the water $3_{1,3}$–$2_{2,0}$ line at $\nu = 183.310$ GHz and the $H^{13}CO^+$ 2–1 line at $\nu = 173.507$ GHz, respectively, and two continuum spws centered at 172.0 and 185.5 GHz with a 1.875 GHz bandwidth each. Each of the two line spws has a bandwidth of 117 MHz and a native spectral resolution of 122 kHz ($\sim$0.2 km s^{-1}) for the H_2O spw and 30.5 kHz (0.05 km s^{-1}) for the $H^{13}CO^+$ spw. After the ALMA pipeline cross calibration, we self-calibrated the data following the pipeline designed for the exoALMA Large Program

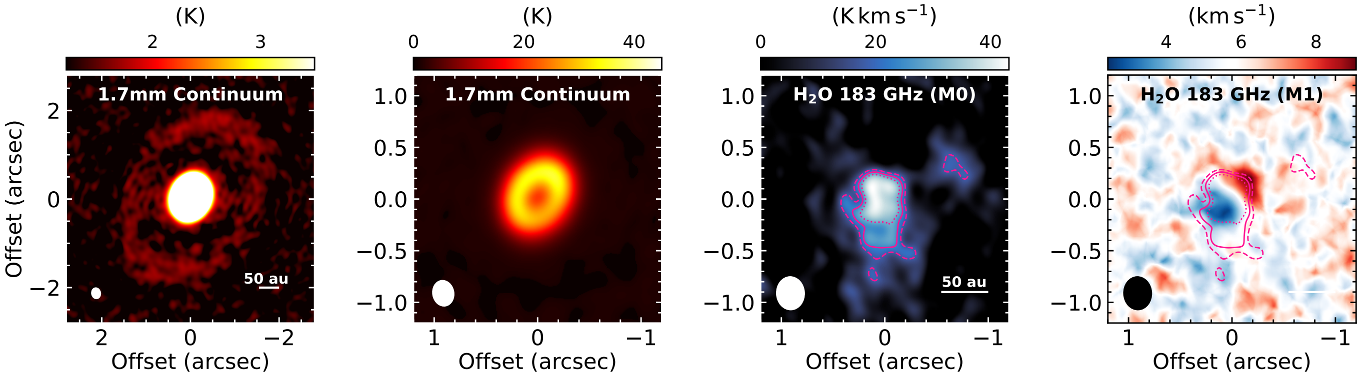

Figure 1. First and second panels: 1.7 mm continuum maps of the HD 100546 disk showing the faint outer ring (first) and a zoom-in on the inner ring (second). Third panel: integrated intensity map of the H_2O 183 GHz line emission. The intensity is expressed as velocity integrated brightness temperature. Pink lines show 3σ, 4σ, and $5\ \sigma$ contours, where σ is evaluated as standard deviation inside an annulus between 2″.3 and 4″.0. Fourth panel: intensity-weighted velocity map of the 183 GHz water line. The color scale is centered at the systemic velocity of 5.7 km s^{-1} (white color). The ellipse in the bottom left of each panel represents the beam.

(R. A. Loomis et al. 2025) and using the `CASA` software version 6.5.4 (CASA Team et al. 2022).

3.1. Self-calibration

After flagging lines within a ±15 km s^{-1} range around the systemic velocity, we averaged the data into 125 MHz wide channels. We applied a first round of phase-only self-calibration to individual EBs, combining spws and scans on EB-long time intervals. We then performed a *uv*-plane alignment as described by R. A. Loomis et al. (2025). The flux rescaling was not performed at this stage of the self-calibration since phase decoherence was found in the data (see R. A. Loomis et al. 2025 for more details). We then concatenated all EBs and applied self-calibration iteratively on progressively shorter time intervals (EB-long, 360 s, 120 s, 60 s, 18 s, and 6s). Only spws and polarizations (no scans) were combined for time intervals shorter than 360 s. Phase self-calibration was performed using models produced through `tclean`, cleaning down to 6σ. An elliptical mask was used during the cleaning, with position angle (PA) PA = 146°.0, a major axis of 2″.5 to include the faint outer ring at ∼200 au, and a minor axis of 2″.5 × cos(i), where i = 41°.7 is the disk inclination (A. S. Booth et al. 2024).

Phase self-calibration improved phase coherence, and flux rescaling was not necessary since flux offsets among different EBs were within 4%. We therefore proceeded with two rounds of amplitude self-calibration, using EB-long and scan-long intervals, respectively, and combining spws and polarizations. For this step, we cleaned down to 1σ. We then applied the gain solutions and phase shifts (in the original order) to the full data set, including spectral lines. Finally, we binned the data into 30 s intervals and performed the continuum subtraction using the `uvcontsub` task. We report a continuum flux of 290 mJy inside the deprojected circular mask used during the self-calibration, a noise rms of 21.5 μJy beam^{-1}, and a peak signal-to-noise ratio (S/N) of 2240 at the end of the self-calibration.

Particular care was taken to estimate the noise rms in the water spw, because of the low transmission caused by the atmospheric telluric line of water. The spectrum of the rms and its impact on the water spectrum are discussed in detail in Appendix A.

3.2. Imaging

The analyses presented in this work were applied to spectral cubes of the water line reconstructed through the `CASA` software (CASA Team et al. 2022) using the `tclean` task (J. A. Högbom 1974; T. J. Cornwell 2008). We used the `multiscale` deconvolver with scales [0, 5, 10, 20, 30] pixels, a pixel size of 0″.01, and a flux threshold of 3σ. To place the CLEAN components, we used the same elliptical mask built for the self-calibration and used to image the continuum.

To find the best balance between sensitivity and spatial resolution, we imaged the line with `Briggs` weighting spanning a range of robust parameters between 0.5 (beam size = 0″.25 × 0″.20, rms ∼ 8 mJy beam^{-1}) and 2.0 (beam size = 0″.32 × 0″.27, rms ∼ 5 mJy beam^{-1}). However, note that the rms varies substantially in the spectral range of the water emission; see Appendix A for more details. Similarly, to find the best balance between spectral resolution and S/N, we imaged the cube with a channel width of 0.6 and 1.2 km s^{-1}. For the results presented in this Letter, we used cubes both with a channel width of 0.6 and 1.2 km s^{-1} and imaged with a robust parameter of 0.5 and 2.0. Figure 5 in Appendix B shows the channel maps of the water line spectral cube, imaged with natural weighting and a channel width of 1.2 km s^{-1}. We applied a correction for the so-called Jorsater–van Moorsel (JvM) effect (S. Jorsater & G. A. van Moorsel 1995) following I. Czekala et al. (2021), to correctly recover the flux of the water line.

3.3. Moment Maps, Radial Profile, and Spectrum

We calculated the integrated intensity map, shown in the middle panel of Figure 1, from the JvM-corrected cube imaged with natural weighting to maximize the sensitivity. We integrated the cube between −6.3 and 13.5 km s^{-1}, after visual inspection of the data with no additional masking, using the `bettermoments` package (R. Teague & D. Foreman-Mackey 2019). The water integrated intensity (moment 0) map is compared to the continuum one in Figure 1. Most of the water emission originates from within the bright continuum ring at ∼15 au, while there is a fainter azimuthally asymmetric component emitting from outside the continuum ring at ∼85 au toward the south/west. The right panel of Figure 1 shows the intensity-weighted velocity map, obtained by

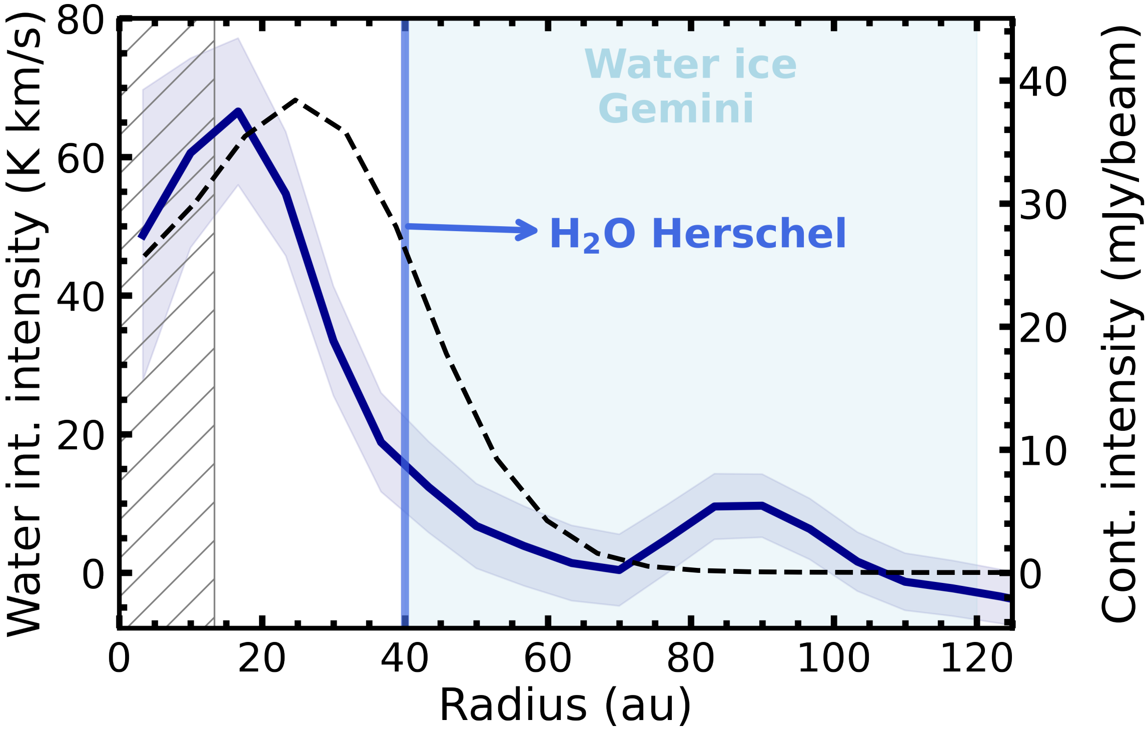

Figure 2. Radial profile of the integrated intensity of the water emission (blue curve) compared to the continuum one (dashed black curve). The blue shaded area shows the uncertainty on the water radial profile. The light blue region indicates the radial extent of the 3 μm water ice absorption band from Gemini observations (M. Honda et al. 2016), and the vertical blue line shows the inner edge of the water emission inferred from Herschel observations (E. F. van Dishoeck et al. 2021; L. M. Pirovano et al. 2022). The hatched region corresponds to the beam semimajor axis of the water cube used to extract the profile. The negative trend of the radial profile beyond 100 au seems to be an artifact due to negative side lobes in the point spread function (PSF).

integrating in the same velocity range used to calculate the moment 0 map. The (moment 1) map shows the typical blue- and redshifted pattern around the systemic velocity of 5.7 km s^{-1}, expected for a disk in Keplerian rotation.

We calculated the water line flux to be 469 ± 165 mJy km s^{-1} by spatially integrating the velocity integrated intensity map inside an elliptical mask with a major axis of 100 au and a minor axis of 100 × cos(i), using the disk geometrical parameters (PA $= 146^\circ\!.0$ and $i = 41^\circ\!.7$) from A. S. Booth et al. (2024). The uncertainty is evaluated as the standard deviation of the flux measured in the same elliptical mask used to evaluate the line flux but outside the emitting area of the integrated intensity map. We took the maximum number of ellipses that was possible to be placed on the image without overlap, performing the procedure on images that are not primary beam corrected, to ensure uniform noise. The flux was extracted from the JvM-corrected cube to avoid overestimating the line flux, while the uncertainty was evaluated from the non-JvM corrected image to avoid underestimating the noise (L. Rampinelli et al. 2024).

From the integrated intensity map of the water emission, we extracted the radial profile of the integrated intensity, shown in Figure 2, using the `GoFish` package (R. Teague 2019). The uncertainty on the radial profile was extracted as

$$\sigma_{\text{radial profile}} = \frac{\sigma_{\text{chan}} \cdot \Delta v \cdot N_{\text{chan}}}{\sqrt{N_{\text{beam/bin}}}}, \quad (1)$$

where σ_{chan} is the standard deviation over the first five and last five channels of the cube used to extract the moment 0 map, Δv is the channel width, N_{chan} is the number of channels over which we integrated to extract the moment 0, and $N_{\text{beam/bin}}$ is the number of beams in each annulus over which we calculated the radial profile of the integrated intensity (which is set to 1 if $N_{\text{beam/bin}} < 1$).

We show the radial profile obtained from the cube imaged with a robust parameter of 0.5 in favor of a higher spatial resolution to highlight possible radial features. The inner peak of the water emission coincides with the inner edge of the dust cavity wall, visible from the comparison of the solid blue and dashed black profiles in Figure 2. The outer azimuthally asymmetric emission observed in the integrated intensity map in Figure 1 is also visible in the radial profile in Figure 2, which shows an outer emission bump peaking at ~85 au. We will further discuss the emission morphology of water vapor in Section 4.

We extracted the disk-integrated spectrum from the cube imaged with natural weighting, using the `GoFish` package (R. Teague 2019). The water line spectrum obtained by integrating over the elliptical mask used to extract the water flux is shown in the left panel of Figure 3. The spectrum shows the typical double-horn feature expected for a Keplerian disk, centered at the systemic velocity of 5.7 km s^{-1} and indicated by the vertical dashed red line. The S/N associated with the peak of the spectrum is 2.6. The uncertainty is 30 mJy, and it is evaluated as a standard deviation of the 88 signal-free velocity bins (blue error bar in the top right corner of Figure 3). We then extracted the spectrum from the same region but correcting for the Keplerian rotation of the disk (R. Teague 2019), as shown in the right panel of Figure 3. The spectral shifting boosts the peak S/N to 5.7, with the uncertainty decreasing to 16.5 mJy.

We highlight that the width of the spectrum in the right panel of Figure 3 should not be interpreted as the water line

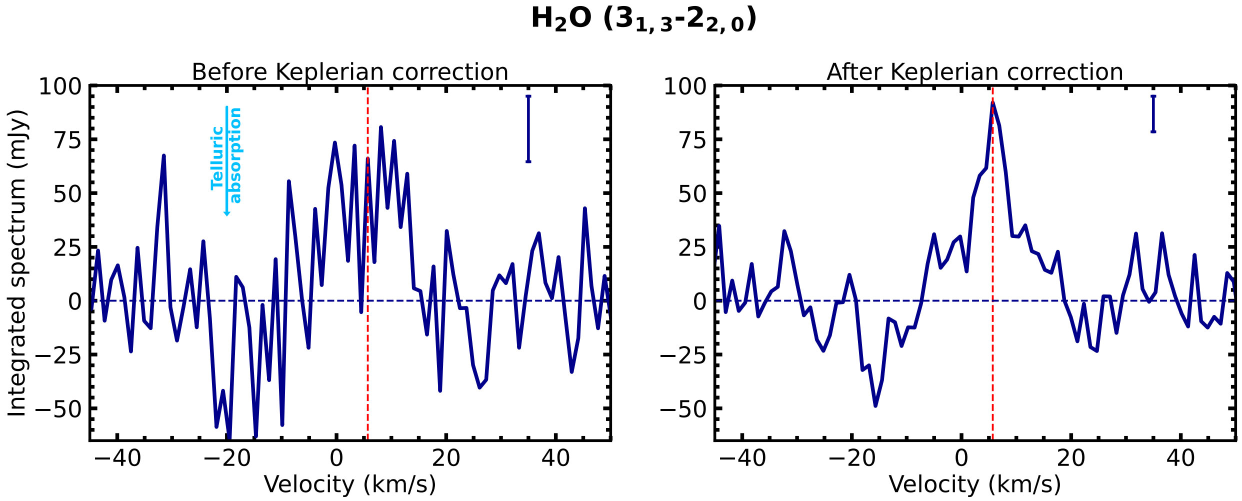

Figure 3. Disk-integrated spectrum of the H_2O line, extracted from a deprojected circle with a radius of 100 au (left panel), and after correcting for the Keplerian rotation (right panel). The vertical red dashed line indicates the systemic velocity of 5.7 km s^{-1}, while the blue line at the top right side of each panel is the uncertainty. The dip in the spectrum in the left panel at ~-21 km s^{-1} is due to the low transmission at the peak of the atmospheric telluric water line (see Appendix A for details on the bandpass calibration and its effect on the retrieved water spectra).

width, since it is affected both by beam and spectral smearing due to the limited spatial (beam major axis ∼35 au) and spectral (channel width = 1.2 km s^{-1}) resolution of the cube used to extract it. Moreover, additional sources of uncertainty possibly affecting the Keplerian shift are associated to the assumed geometrical parameters (inclination, PA, and emitting surface), stellar mass, and distance of the source.

4. Discussion

The presented observations show the first spatially resolved detection of the main water vapor isotopologue with ALMA in a transition disk. As anticipated in Section 3.3, the water emission at 183.31 GHz shows an inner bright peak at 15 au. In the following sections, we discuss this result in light of the previous dust and line observations of the disk around HD 100546.

4.1. Water Vapor at the Warm Cavity Wall

The peak of the radial profile of the water integrated intensity in Figure 2 is at the cavity wall of the dust disk, at a radius of (15 ± 5) au. The astrometric accuracy on the peak of the profile in Figure 2 is estimated as $\theta_{\rm FWHM}/{\rm S/N}/0.9$ (see P. Cortes et al. 2025), which implies a 2σ offset between the disk cavity wall at ∼15 au and the peak of the dust ring at ∼25 au. We suggest this emission originates from thermally desorbed water at the snow line.

The location of the water snow line is typically only a few astronomical units away from the central star for T Tauri stars and within ∼10 au also for warmer Herbig disks, as the high water binding energy implies a high sublimation temperature of ∼150 K. However, HD 100546 is a transition disk around a Herbig star, with an intrinsically warmer temperature structure (M. Leemker et al. 2022) and a central dust and gas cavity (J. E. Pineda et al. 2019; S. Pérez et al. 2020; L. Wölfer et al. 2023; A. S. Booth et al. 2024). These physical conditions result in an efficiently irradiated cavity wall reaching temperatures higher than the water sublimation temperature (M. Leemker et al. 2024) and pushing the water snow line to larger radii. This is also consistent with the thermochemical model from M. Leemker et al. (2024) predicting the water snow line to be located at ∼15 au at the cavity wall.

While less severe than at IR wavelengths (M. Leemker et al. 2025a), optically thick dust can partially hide water vapor emission. The rapid drop outside ∼20 au in the radial profile of the water integrated intensity in Figure 2 could also be a consequence of the optically thick dust ring at ∼25 au, instead of water freeze-out. However, high-spatial-resolution ALMA band 7 continuum observations show that the peak of the continuum brightness temperature (at ∼25 au) is ∼80 K, well below the water sublimation temperature of ∼150 K, suggesting that the water snow line is located at the inner edge of the dust ring at ∼15 au. This is also supported by radiative transfer models showing that the midplane dust temperature steeply drops below ∼150 K at the cavity wall (J. E. Pineda et al. 2014, 2019; L. Keyte et al. 2023; M. Leemker et al. 2024).

The thermal desorption origin of the observed water emission at the dust cavity wall is supported by the fact that multiple oxygen-rich molecules including methanol have been suggested to thermally sublimate in the HD 100546 disk (A. S. Booth et al. 2024; L. Evans et al. 2025).

To summarize, the evidence outlined above points to the conclusion that the water snow line is located at the cavity edge of the dust disk at ∼15 au in the HD 100546 disk.

4.2. Comparison with Herschel Observations

Previous observations of water vapor in this source with Herschel only revealed cold water transitions ($E_{\rm up}$ = 53 and 61 K), associated to the photodesorption layer outside ∼40 au. Hot ($E_{\rm up}$ > 300 K) and warm ($E_{\rm up} \sim 200-300$ K) water lines were also targeted with Herschel but not detected in the disk of HD 100546 (E. F. van Dishoeck et al. 2021; L. M. Pirovano et al. 2022).

The hot water lines with high $E_{\rm up}$ ($\gtrsim$300 K) are expected to trace the hot water reservoir produced in the gas phase in the upper layers and inside the dust cavity (see Section 1), where photodissociation limits the water abundance. Water self-shielding has been shown to mitigate this effect when the water column density is high ($\gtrsim 10^{18}$ cm^{-2}, T. Bethell & E. Bergin 2009; A. D. Bosman et al. 2022; J. K. Calahan et al.

2022). However, HD 100546 is a transition disk with a large dust cavity that is also depleted in gas. The right panel of Figure 6 in Appendix C represents the radial profile of the water column density from the thermochemical model by M. Leemker et al. (2024), which shows that the water column density in the disk cavity is expected to be low enough to allow efficient photodissociation. We highlight that this model includes photodissociation only in the vertical direction and not in the radial one. The nondetection of the hot Herschel lines with $E_{\rm up} = 432$, 552, and 843 K, which trace the hot water reservoir in the upper layers and inside the cavity, can be thus explained by the efficient photodissociation (L. M. Pirovano et al. 2022).

On the other hand, the water column density is higher at the disk cavity edge at ∼15 au where the water snow line is expected to be located (see the right panel of Figure 6), thus favoring water self-shielding against photodissociation. The warm Herschel lines with $E_{\rm up} = 194$, 300, and 323 K and the ALMA line with $E_{\rm up} = 205$ K, which are expected to trace closer to the water snow line, are therefore expected to be detected.

These warm Herschel lines could go undetected if they are subthermally excited, as their critical density is higher than the local gas density. The left panel of Figure 6 shows the critical density of the Herschel lines presented by L. M. Pirovano et al. (2022; solid lines) and of the ALMA 183 GHz line (dashed line), as a function of temperature, calculated following A. Faure et al. (2024), under the optically thin assumption, and neglecting absorption, stimulated emission, and background emission (see Appendix C). The critical densities of the warm Herschel lines with $E_{\rm up} = 194$, 300, and 323 K are $\sim 10^9$ cm^{-3} at ∼150 K and approximately a factor of 3 higher than the ALMA line. However, we highlight that these warm Herschel lines have high Einstein coefficients $\log_{10}(A_{\rm ul}\,[{\rm s}^{-1}]) = -0.59$, -0.48, and -0.61 and are therefore expected to be optically thicker than the ALMA 183 GHz line with $\log_{10}(A_{\rm ul}\,[{\rm s}^{-1}]) = -5.44$. In the optically thick regime, photon trapping can consistently lower the critical density (Y. L. Shirley 2015). This, together with the fact that the gas density is expected to be $>10^9$ cm^{-3} at the disk cavity wall (M. Leemker et al. 2024), suggests that subthermal excitation cannot explain the nondetection of the warm Herschel lines against the detection of the ALMA line.

The nondetection of warm water vapor with Herschel could be due to the high continuum optical depth of the inner dust ring at Herschel wavelengths with respect to ALMA, potentially hiding water emission in this region in the far infrared (FIR). On the other hand, the optical depth of dust is much lower at ALMA wavelengths, thus allowing the detection of the warm 183 GHz ALMA line ($T \gtrsim 150$ K) emitting at the dust cavity edge.

Finally, we report a marginal detection (peak S/N = 4 in the channel maps) of azimuthally asymmetric water emission peaking at ∼85 au in the western and southern sides of the disk (see the 8.10 km s^{-1} channel in Figure 5 of Appendix B). In this context, we note that HD 100546 has a dynamically active disk with large-scale spiral arms (A. Garufi et al. 2016). The faint bump is also visible in the radial profile of the integrated intensity (Figure 2), but the S/N is too low (∼2) to robustly conclude regarding its significance. Interestingly, photodesorption of water ice has been proposed in the cold outer gap between the two dust rings at ∼25 and ∼200 au (M. Honda et al. 2016; L. M. Pirovano et al. 2022).

4.3. Water Vapor Emission and the Molecular Complexity of HD 100546

A. S. Booth et al. (2024) presented ALMA line emission observations of a rich sample of molecular tracers in the disk of HD 100546, most of them showing a double-ringed emission similar to what is observed in ALMA continuum observations. M. Leemker et al. (2024) showed that chemistry rather than the underlying density structure is responsible for the observed molecular rings. In particular, oxygen- and carbon-rich molecules show the peak of the emission just inside or outside the inner dust ring at ∼25 au, respectively. In addition, most of the molecules show a second peak just outside the outer dust ring at ∼200 au (A. S. Booth et al. 2024). This morphology suggests a radially varying C/O ratio, higher at the dust rings, where C_2H and CN show bright emission (M. Leemker et al. 2024). This picture is supported by the detection of methanol and SO inside the inner dust cavity (L. Evans et al. 2025), and it is also consistent with the water morphology presented in this work. As shown in Figure 2, the inner bright peak of water emission at ∼15 au is just inside the inner dust ring, while the outer faint water emission peaking at ∼85 au is within the gas gap, both anticorrelating with the dust rings where the C/O ratio is proposed to be above 1 (M. Leemker et al. 2024).

The observed water emission morphology is expected to anticorrelate with the HCO^+ emission, the latter being a major destruction pathway for water (T. G. Phillips et al. 1992; E. A. Bergin et al. 1998; M. Leemker et al. 2021). HCO^+ shows a centrally peaked emission and an outer ring colocated with the outer dust ring (A. S. Booth et al. 2024). The observed faint water emission at ∼85 au is therefore consistent with a region of fainter HCO^+ emission. While the radial profile of the water integrated intensity in Figure 2 shows marginal evidence of a decreasing trend inside ∼15 au, the spatial resolution of both the H_2O and HCO^+ observations does not allow us to robustly conclude about their anticorrelation inside the inner dust cavity. The marginal inner drop in H_2O could also be due to a drop in the gas density, as HD 100546 shows an inner gas cavity. On the other hand, HCO^+ is a good tracer of the ionization rate, and if it became optically thicker than water in the inner gas cavity, it would follow the drop in the gas density (M. Leemker et al. 2024). However, we highlight that the detection of water vapor is consistent with the low HCO^+/CO column density ratio extracted for the HD 100546 disk (A. S. Booth et al. 2024), which could either result from a low ionization rate or the presence of gas-phase water.

5. Conclusions

In this work, we present the first spatially resolved observations of the main water vapor isotopologue with ALMA in a transition disk. Our observations of the HD 100546 disk show

1. Water emission peaking at the warm cavity wall of the transition disk. The high temperature in the dust cavity induced by the intense radiation field pushes the snow line to larger radii, allowing water to thermally desorb at the inner edge of the dust cavity;

2. The first *direct* image of the water snow line in a protoplanetary disk from spatially resolved observations of the main water isotopologue;
3. The gas-phase distribution of water vapor, complementing previous observations of O-rich COMs in the transition disk. This reveals that planets forming inside the warm cavity of the transition disk are exposed to a water-rich chemistry that can leave a crucial imprint on the atmospheric composition of planets forming in the disk; and
4. The potential of ALMA for tracing the water vapor distribution in planet-forming disks, thanks to the extremely favorable weather conditions reached at the observatory site, and the high resolution and sensitivity that can be achieved.

Acknowledgments

This Letter makes use of the following ALMA data: ADS/JAO.ALMA 2023.1.01431.S.

ALMA is a partnership of ESO (representing its member states), NSF (USA) and NINS (Japan), together with NRC (Canada), MOST and ASIAA (Taiwan), and KASI (Republic of Korea), in cooperation with the Republic of Chile. The Joint ALMA Observatory is operated by ESO, AUI/NRAO and NAOJ.

L.R., S.F., and M.L. are funded by the European Union (ERC, UNVEIL, 101076613). Views and opinions expressed are, however, those of the authors only and do not necessarily reflect those of the European Union or the European Research Council. Neither the European Union nor the granting authority can be held responsible for them. S.F. also acknowledges financial contribution from PRIN-MUR 2022YP5ACE. A.I. acknowledges support from the National Aeronautics and Space Administration under grant No. 80NSSC18K0828. P.C. acknowledges support by the ANID BASAL project FB210003. M.B. has received funding from the European Research Council (ERC) under the European Union's Horizon 2020 research and innovation program (PROTOPLANETS, grant agreement No. 101002188). L.T. acknowledges financial support from the European Research Council via the ERC Synergy Grant "ECOGAL" (project ID 855130).

Facility: ALMA.

Software: `CASA` v6.5.4 (CASA Team et al. 2022), `numpy` (C. R. Harris et al. 2020), `matplotlib` (J. D. Hunter 2007), `bettermoments` (R. Teague & D. Foreman-Mackey 2019), `gofish` (R. Teague 2019).

Appendix A
Noise in the Water spw

We report a spectral dependence of the noise rms in the water spw. The left panel of Figure 4 shows the noise rms evaluated inside a circle with a radius of 500 au, as a function of velocity. The noise rms was extracted from non-JvM corrected cubes (to avoid underestimating the noise) imaged with natural weighting and a channel with of 1.2 km s^{-1}. The vertical dotted line shows the systemic velocity of 5.7 km s^{-1} (in the LSRK velocity frame), while the vertical dashed line corresponds to a velocity of 0 km s^{-1} in the topocentric frame. The x-axes show the velocity in LSRK (bottom) and topocentric frame (top). The strong spectral dependence of the noise level is due to the lower transmission at the peak of the water telluric line, which is shifted with respect to the LSRK systemic velocity of the science target, peaking at ~ -21 km s^{-1} in the LSRK frame. As expected, the peak of the noise rms is correctly centered at 0 km s^{-1} in the topocentric frame, with the Lorentzian wings clearly recognizable throughout the spw. The observed velocity shift in the LSRK frame with respect to the topocentric frame at the location of ALMA is consistent with the observing dates and times and with the source coordinates. In particular, the three EBs were taken on 2024 June 30 at 20:55 UTC, 2024 June 30 at 22:24 UTC, and 2024 July 2 at 21:07 UTC. The small difference in dates only induces a small shift in LSRK velocity.

EB0 and EB1 were taken in worse weather conditions than EB2, with the former showing a mean PWV of 0.4 mm and the latter, 0.2 mm. The noise rms is significantly higher for EB0 and EB1 than for EB2 (see the left panel of Figure 4), due to the exponential dependence with the atmospheric transmission within the telluric line. Due to the lower S/N during the first

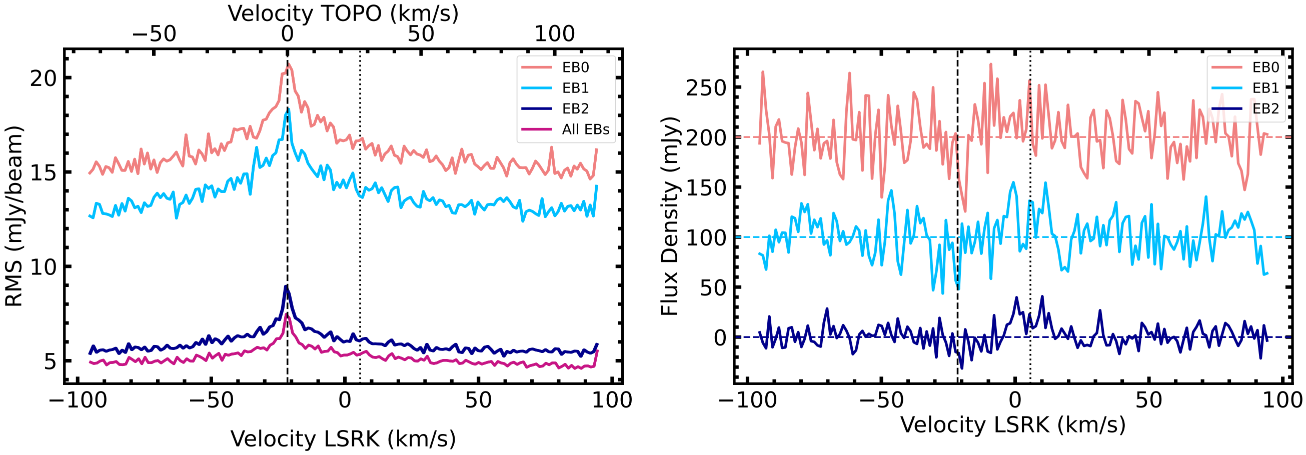

Figure 4. Left: rms as a function of velocity extracted from a circle with a 500 au radius for the three EBs and combination of all EBs. Right: water spectrum extracted from a circle with a 50 au radius for the three EBs (EB0 and EB1 have been shifted by 100 and 200 mJy for clarity). Non-JvM corrected cubes imaged with natural weighting and a channel width of 1.2 km s^{-1} were used. The vertical dashed lines correspond to the systemic velocity in the LSRK frame, and the vertical dotted lines correspond to $v = 0$ km s^{-1} in the TOPO frame.

two EBs, the bandpass calibration of the water spw on EB0 and EB1 was performed averaging over 10 and 6 velocity channels, respectively, while no averaging was applied to EB2. This has a direct consequence in the retrieved continuum-subtracted spectrum of the water spw. The right panel of Figure 4 shows the spectrum of the water line for the three EBs separately (EB0 and EB1 were shifted up for clarity), inside a circle with a 50 au radius. The spectra show a small dip (also visible in Figure 3) at the peak of the spw rms. As expected from the different weather conditions and spectral averaging during bandpass calibration for EB0 and EB1, the spectrum from EB2 shows the smallest dip.

We highlight that this effect could be particularly important when scheduling water observations with ALMA (in particular for the 183 GHz water line), depending on the observing date and science target, since the trough in the atmospheric transmission could partially overlap with the water line of the astrophysical source of interest, thus resulting in both an elevated rms level and artificial absorption features.

Appendix B
Water Channel Maps

Figure 5 shows the channel maps of the detected water line in the HD 100546 disk. The cube was imaged with natural weighting and a channel width of 1.2 km s^{-1} (see Section 3.2 for more details on the imaging procedure).

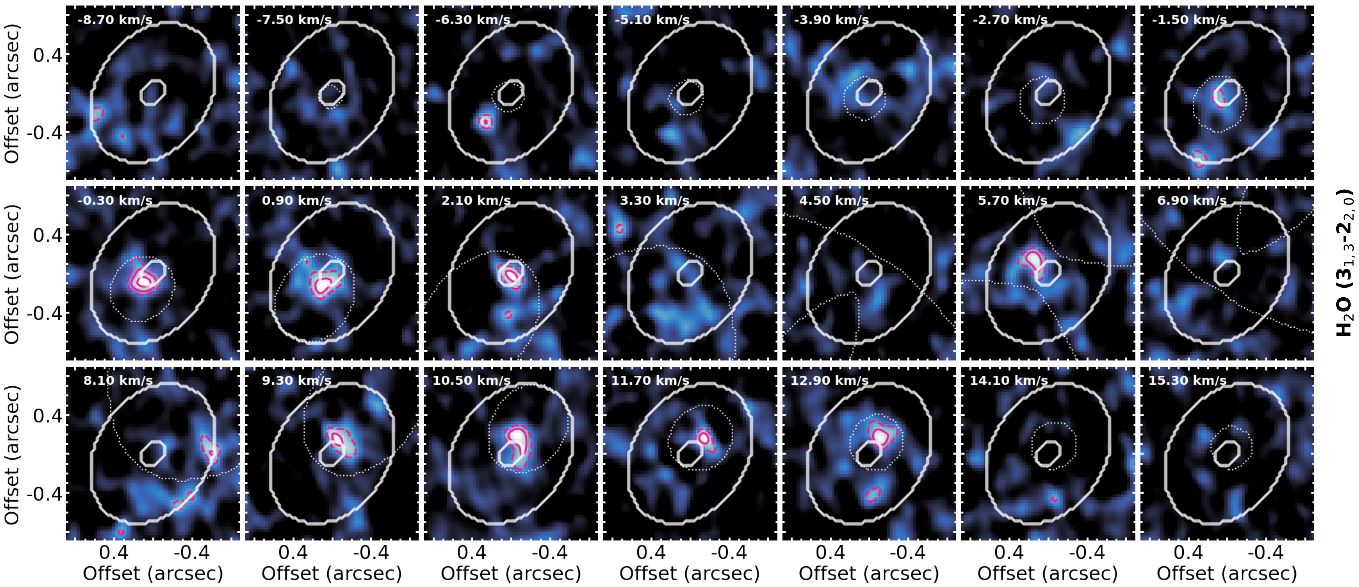

Figure 5. Channel maps of the water line at 183 GHz. The systemic velocity is 5.7 km s^{-1}. White ellipses correspond to the location of the two peaks in the radial profile (see Figure 2) at $R = 15$ and 85 au. Pink contours show 3σ, 4σ, and 5σ levels, where σ is evaluated as standard deviation inside an annulus between 250 and 450 au for each channel. The white dotted contours show the expected Keplerian pattern.

Appendix C
Water Observations with Herschel and ALMA

The left panel of Figure 6 shows the critical density of the Herschel lines in L. M. Pirovano et al. (2022, solid lines) and of the ALMA 183 GHz line (dashed line), as a function of temperature. The profiles are colored based on their upper state energy. The critical densities are calculated following A. Faure et al. (2024):

$$n_{\rm crit} = \frac{\sum_k A_{jk}}{\sum_k \kappa_{jk}} = \frac{\sum_k A_{jk}}{\sum_{k<j}\gamma_{jk} + \sum_{k>j}\frac{g_k}{g_j}\gamma_{kj}\, e^{-(E_k-E_j)/kT}}, \qquad \text{(C1)}$$

where A_{jk} is the Einstein coefficient of the spontaneous emission and γ_{jk} is the collision rate out of level j into level k. The upward collision rate γ_{jk} is related to the downward γ_{kj} one as follow (Y. L. Shirley 2015):

$$\gamma_{jk} = \frac{g_k}{g_j}\gamma_{kj}\, e^{-(E_k-E_j)/kT}, \qquad \text{(C2)}$$

where g is the degeneracy, E is the energy, and T is the kinetic temperature. The critical density is calculated under the assumption of optically thin water emission and neglecting absorption, stimulated emission, and background emission.

The right panel of Figure 6 shows the radial profile of the water column density obtained from the thermochemical model built by M. Leemker et al. (2024) using DALI (S. Bruderer et al. 2012; S. Bruderer 2013) for the HD 100546 disk. We highlight that this model aimed at reproducing the emission morphology of a variety of molecules detected with ALMA, in particular, CO isotopologues, HCN, CN, C_2H, NO, and HCO^+, but it was not specifically built to reproduce the water emission and observations in this source.

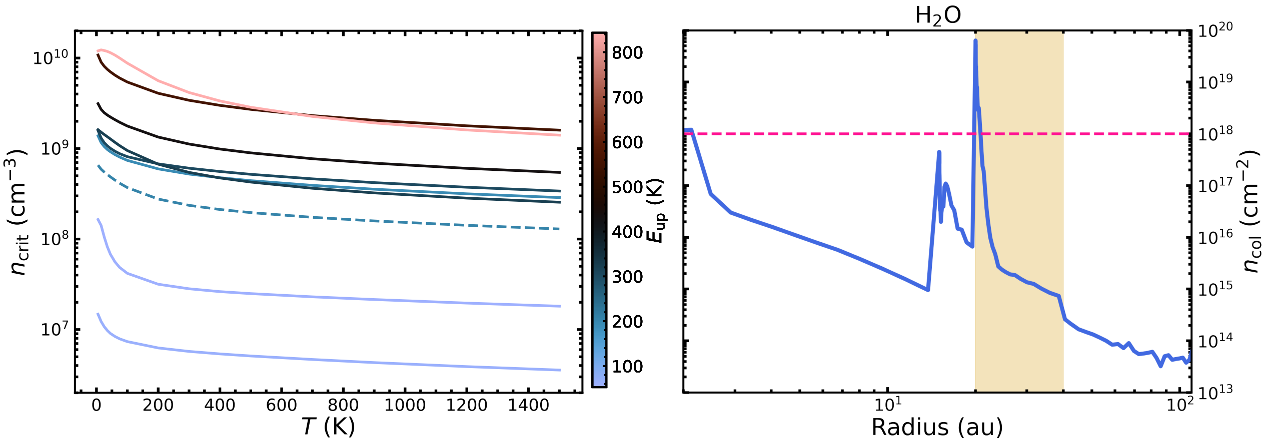

Figure 6. Left: critical density as a function of temperature for the Herschel lines included in L. M. Pirovano et al. (2022, solid lines) and the ALMA 183 GHz line (dashed). The color bar shows the upper state energies of each transition. Right: water column density from the DALI model of the HD 100546 disk from M. Leemker et al. (2024). The pink horizontal line indicates the density above which water self-shielding is expected to be important. The brown shaded region indicates the dust ring between 20 and 40 au.

ORCID iDs

Rampinelli Luna https://orcid.org/0009-0001-2795-8468
Facchini Stefano https://orcid.org/0000-0003-4689-2684
Leemker Margot https://orcid.org/0000-0003-3674-7512
Isella Andrea https://orcid.org/0000-0001-8061-2207
Curone Pietro https://orcid.org/0000-0003-2045-2154
Benisty Myriam https://orcid.org/0000-0002-7695-7605
Humphreys Elizabeth https://orcid.org/0000-0001-9549-6421
Testi Leonardo https://orcid.org/0000-0003-1859-3070

References

Andreu, A., Coutens, A., Cruz-Sáenz de Miera, F., et al. 2023, A&A, 677, L17
Banzatti, A., Pascucci, I., Bosman, A. D., et al. 2020, ApJ, 903, 124
Banzatti, A., Pontoppidan, K. M., Carr, J. S., et al. 2023a, ApJL, 957, L22
Banzatti, A., Pontoppidan, K. M., Pére Chávez, J., et al. 2023b, AJ, 165, 72
Banzatti, A., Pontoppidan, K. M., Salyk, C., et al. 2017, ApJ, 834, 152
CASA Team, Bean, B., Bhatnagar, S., Castro, S., et al. 2022, PASP, 134, 114501
Bergin, E. A., Hogerheijde, M. R., Brinch, C., et al. 2010, A&A, 521, L33
Bergin, E. A., Melnick, G. J., & Neufeld, D. A. 1998, ApJ, 499, 777
Bethell, T., & Bergin, E. 2009, Sci, 326, 1675
Booth, A. S., Ilee, J. D., Walsh, C., et al. 2023, A&A, 669, A53
Booth, A. S., Leemker, M., van Dishoeck, E. F., et al. 2024, AJ, 167, 164
Bosman, A. D., Bergin, E. A., Calahan, J., & Duval, S. E. 2022, ApJL, 930, L26
Brittain, S. D., Najita, J. R., & Carr, J. S. 2019, ApJ, 883, 37
Bruderer, S. 2013, A&A, 559, A46
Bruderer, S., van Dishoeck, E. F., Doty, S. D., & Herczeg, G. J. 2012, A&A, 541, A91
Calahan, J. K., Bergin, E. A., & Bosman, A. D. 2022, ApJL, 934, L14
Casassus, S., & Pérez, S. 2019, ApJL, 883, L41
Cornwell, T. J. 2008, ISTSP, 2, 793
Cortes, P., Carpenter, J., Kameno, S., et al. 2025, ALMA Cycle 12 Technical Handbook, ALMA Doc. 12.3, v1.5, Zenodo, doi:10.5281/zenodo.14933753
Cridland, A. J., Pudritz, R. E., & Alessi, M. 2016, MNRAS, 461, 3274
Currie, T., Cloutier, R., Brittain, S., et al. 2015, ApJL, 814, L27
Czekala, I., Loomis, R. A., Teague, R., et al. 2021, ApJS, 257, 2
Drążkowska, J., Bitsch, B., Lambrechts, M., et al. 2023, ASPC, 534, 717
Eistrup, C., Walsh, C., & van Dishoeck, E. F. 2018, A&A, 613, A14
Evans, L., Booth, A. S., Walsh, C., et al. 2025, ApJ, 982, 62
Facchini, S., Testi, L., Humphreys, E., et al. 2024, NatAs, 8, 587
Faure, A., Żółtowski, M., Wiesenfeld, L., Lique, F., & Bergeat, A. 2024, MNRAS, 527, 3087
Fedele, D., Toci, C., Maud, L., & Lodato, G. 2021, A&A, 651, A90
Follette, K. B., Rameau, J., Dong, R., et al. 2017, AJ, 153, 264
Gaia Collaboration, Prusti, T., de Bruijne, J., H., J., Brown, A. G. A., et al. 2016, A&A, 595, A1
Gaia Collaboration, Vallenari, A., Brown, A. G. A., Prusti, T., et al. 2023, A&A, 674, A1
Garufi, A., Quanz, S. P., Schmid, H. M., et al. 2016, A&A, 588, A8
Harris, C. R., Millman, K. J., van der Walt, S. J., et al. 2020, Natur, 585, 357
Högbom, J. A. 1974, A&AS, 15, 417
Hogerheijde, M. R., Bergin, E. A., Brinch, C., et al. 2011, Sci, 334, 338
Honda, M., Kudo, T., Takatsuki, S., et al. 2016, ApJ, 821, 2
Hunter, J. D. 2007, CSE, 9, 90
Jorsater, S., & van Moorsel, G. A. 1995, AJ, 110, 2037
Kamp, I., Henning, T., Arabhavi, A. M., et al. 2023, FaDi, 245, 112
Keyte, L., Kama, M., Booth, A. S., et al. 2023, NatAs, 7, 684
Leemker, M., Booth, A. S., van Dishoeck, E. F., Wölfer, L., & Dent, B. 2024, A&A, 687, A299
Leemker, M., Booth, A. S., van Dishoeck, E. F., et al. 2022, A&A, 663, A23
Leemker, M., Facchini, S., & Curone, P. 2025a, arXiv:2511.16737
Leemker, M., Tobin, J. J., Facchini, S., et al. 2025b, NatAs, 9, 1486
Leemker, M., van't Hoff, M. L. R., Trapman, L., et al. 2021, A&A, 646, A3
Loomis, R. A., Facchini, S., Benisty, M., et al. 2025, ApJL, 984, L7
Minissale, M., Aikawa, Y., Bergin, E., et al. 2022, ESC, 6, 597
Morbidelli, A., Lunine, J. I., O'Brien, D. P., Raymond, S. N., & Walsh, K. J. 2012, AREPS, 40, 251
Najita, J. R., Carr, J. S., Pontoppidan, K. M., et al. 2013, ApJ, 766, 134
Notsu, S., Nomura, H., Ishimoto, D., et al. 2017, ApJ, 836, 118
Öberg, K. I., Facchini, S., & Anderson, D. E. 2023, ARA&A, 61, 287
Öberg, K. I., Murray-Clay, R., & Bergin, E. A. 2011, ApJL, 743, L16
Pérez, S., Casassus, S., Hales, A., et al. 2020, ApJL, 889, L24
Phillips, T. G., van Dishoeck, E. F., & Keene, J. 1992, ApJ, 399, 533
Pineda, J. E., Quanz, S. P., Meru, F., et al. 2014, ApJL, 788, L34
Pineda, J. E., Szulágyi, J., Quanz, S. P., et al. 2019, ApJ, 871, 48
Pirovano, L. M., Fedele, D., van Dishoeck, E. F., et al. 2022, A&A, 665, A45
Pontoppidan, K. M., Salyk, C., Blake, G. A., & Käufl, H. U. 2010, ApJL, 722, L173
Rampinelli, L., Facchini, S., Leemker, M., et al. 2024, A&A, 689, A65
Salyk, C., Pontoppidan, K. M., Blake, G. A., Najita, J. R., & Carr, J. S. 2011, ApJ, 731, 130
Schoonenberg, D., & Ormel, C. W. 2017, A&A, 602, A21
Shirley, Y. L. 2015, PASP, 127, 299
Sissa, E., Gratton, R., Garufi, A., et al. 2018, A&A, 619, A160
Teague, R. 2019, JOSS, 4, 1632
Teague, R., & Foreman-Mackey, D., 2019 bettermoments: Line-of-sight velocity calculation, Astrophysics Source Code Library, ascl:1901.009
Temmink, M., van Dishoeck, E. F., Gasman, D., et al. 2024, A&A, 689, A330
Tobin, J. J., van't Hoff, M. L. R., Leemker, M., et al. 2023, Natur, 615, 227
van Dishoeck, E. F., Bergin, E. A., Lis, D. C., & Lunine, J. I. 2014, in Protostars and Planets VI, ed. H. Beuther (Univ. of Arizona), 835
van Dishoeck, E. F., Kristensen, L. E., Mottram, J. C., et al. 2021, A&A, 648, A24
Vioque, M., Oudmaijer, R. D., Baines, D., Mendigutía, I., & Pérez-Martínez, R. 2018, A&A, 620, A128
Wakelam, V., Loison, J. C., Mereau, R., & Ruaud, M. 2017, MolAs, 6, 22
Walsh, C., Daley, C., Facchini, S., & Juhász, A. 2017, A&A, 607, A114
Walsh, C., Juhász, A., Pinilla, P., et al. 2014, ApJL, 791, L6
Woitke, P., Thi, W. F., Kamp, I., & Hogerheijde, M. R. 2009, A&A, 501, L5
Wölfer, L., Facchini, S., van der Marel, N., et al. 2023, A&A, 670, A154